Studies of the Effects of Control Bandwidth and Dark-Hole Size on the HCIT Contrast Performance

*Erkin Sidick, Stuart Shaklan, Kunjithapatham Balasubramanian, and Eric Cady
Jet Propulsion Laboratory, California Institute of Technology, 4800 Oak Grove Drive, Pasadena, CA 91109, USA

ABSTRACT

We have carried out both theoretical and experimental studies of the sensitivity of dark hole contrast to the control bandwidth and dark-hole dimensions in high-contrast broadband stellar coronagraphy. We have evaluated the performance of DM actuator solutions in the presence of occulting mask defects using one to five 2%-wide bands spanning a 10% bandpass. We have also investigated the dependence of the HCIT contrast performance on the size of dark-hole area including large dark holes formed at the Nyquist limit of the DM.

Key words: Coronagraphy, adaptive optics, high-contrast imaging, space telescopes, exoplanets

1. INTRODUCTION

This paper presents both simulated and measured results on the sensitivity of broadband contrast to the control bandwidth and dark-hole dimensions in a Lyot coronagraph implemented on the High-Contrast Imaging Testbed (HCIT) at NASA's Jet Propulsion Laboratory (JPL). This testbed is the Exoplanet Exploration Program's primary platform for experimentation [1-3]. It is used to provide laboratory validation of key technologies as well as demonstration of a flight-traceable approach to implementation. It employs a 48x48 actuator deformable-mirror (DM) and a broadband wavefront correction algorithm called Electric Field Conjugation (EFC) to obtain the required 10^{-10} contrast [4]. To predict the measured contrast performance of the coronagraph, we have carried out simulations by using the measured microscope image of an occulter's transmittance while keeping its phase the same as that of the model, as well as adding some phase values to the measured occulter spots. The laboratory testing was carried out with either a 2%-narrowband or a 10%-broadband light. The simulations were conducted with MACOS (Modeling and Analysis for Controlled Optical Systems) [5], and their results were compared with measurements. We achieved good agreement between the measurement and the simulation in some of the cases investigated. In four earlier papers we reported on the broadband contrast sensitivity to the number and the position of dead actuators, beam walk due to translation of a flat optic in the beam, as well as on the effects of occulter displacement, an opaque spot on the occulter, the controlled dark-hole dimensions, and the various defects of the focal plane mask [6-9]. In a companion paper, we will report the results of our simulations and experiment on the sensitivity of the broadband contrast to one to four pairs of pegged (or frozen) DM actuators [10].

2. DEFINITION OF DARK-HOLE AREA AND MEASURED CONTRAST MAPS

The detailed background information of the Lyot coronagraph used in this study is given in Ref. [7] as well as in our earlier papers and is not repeated here. For the current optical system with only one DM, we carry out wavefront control (WFC) over a region Ω_b, where Ω_b is either a D-shaped dark-hole region bound by $X \geq X_{min}$ and $R \leq R_{max}$, or a rectangular region bound by $[X_{min}\ X_{max}\ Y_{min}\ X_{max}]$, with $X = x/f$, $Y = y/f$, $R = \sqrt{X^2 + Y^2}$, x and y are the horizontal and the vertical position variables on the corresponding image-plane, and f is the focal length. For example, in the studies on the sensitivity of broadband contrast to control bandwidth, we used $[X_{min}, R_{max}] = [3.5\ 11]\lambda/D$ for Ω_b. We evaluate the performance of the HCIT using the normalized intensity,

_____

*Erkin.Sidick@jpl.nasa.gov; Phone 1 818 393-7585; Fax 1 818 393-3290; www.jpl.nasa.gov

$$I_n(x, y) = I(x, y)/I_0, \tag{1}$$

where $I(x, y)$ is the image intensity of the occulted star, and I_0 is the maximum value of the un-occulted star intensity. We keep track of I_b, the mean value of $I_n(x, y)$ inside a "Big" dark-hole region Ω_b defined above.

3. OCCULTER SPOT PHASE

This section supersedes Section 3.4 in Ref. [7]. In that paper, the coherent model was compared to the combined incoherent and coherent estimates of the dark hole. Also, we did not have a model of dust particles in that work. A model of occulter dust particles is included here.

The speckly nature of the observed coherent dark-hole floor, and the simple particle distribution model that produces a similar result, indicate that localized mask errors are the likely cause of the contrast floor. We have measured the transmission (amplitude only, not phase) of the occulter using high resolution microscope images to inform a model and see if a mask characterization measurement can be used to predict dark-hole contrast. Figure 1 is the transmission image of the front side of the occulter, formed by placing a diffuser between the point source and the mask in the HCIT testbed. The vertical yellow-line is at $X = 3.5\lambda/D$, and the red- circle has a radius of $R = 20\lambda/D$; this image roughly corresponds to the area of the occulter used in our experiments.
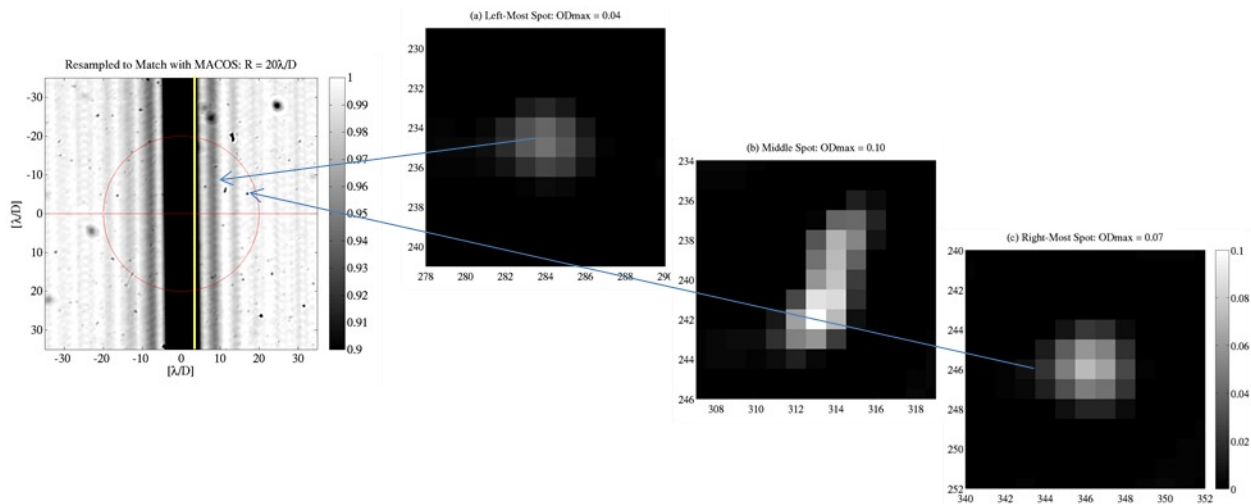

Figure 1. Left: Transmitted amplitude images of occulter's front side. The circle extends to $R = 20\ \lambda/D$ and is positioned where the beam is centered in the experiment. The three spots on the right side of the occulter image are the magnified versions of the three spot images on the left. Pixel pitch in these images is 4.3 μm.

Registration of the dark-hole with the mask was confirmed by the presence of 3 spots roughly horizontally aligned within the upper half of the red circle of Figure 1. These spots lead to the largest residuals in our models and are well aligned with dark-hole residuals.

Contrast predictions for the ideal occulter are well below the measured contrast. When the measured spots are included in the model and treated as simple attenuators (no phase), the contrast is still well below the measurements, as documented in Ref. [9]. We have found that adding a phase term to the spots that varies in proportion to the optical density creates a contrast floor that closely resembles the measured data. However, we presently have no explanation for why the phase term exists, and why a particular value of phase vs. OD works the best. The phase term has the form $\varphi_{spot} \approx \pi \times F_{spot} OD_{spot}$, where F_{spot} is a multiplier, and we tested it with $F_{spot} = 0, 0.5, 1,$ and 1.5, respectively.

To quantitatively understand the distribution of occulter spots on the occulter surface area of interest, we chose a rectangular region whose boundaries are defined by [$x=\pm24\ \lambda/D$, $y=\pm14\ \lambda/D$] with the right side of the box nominally registered with the experimental dark-hole location, as shown in Fig. 2(a). Figure 2(b) shows the histogram of OD values for OD>0.02. The deepest spot OD has a value of ~0.1 and occupies only one pixel.
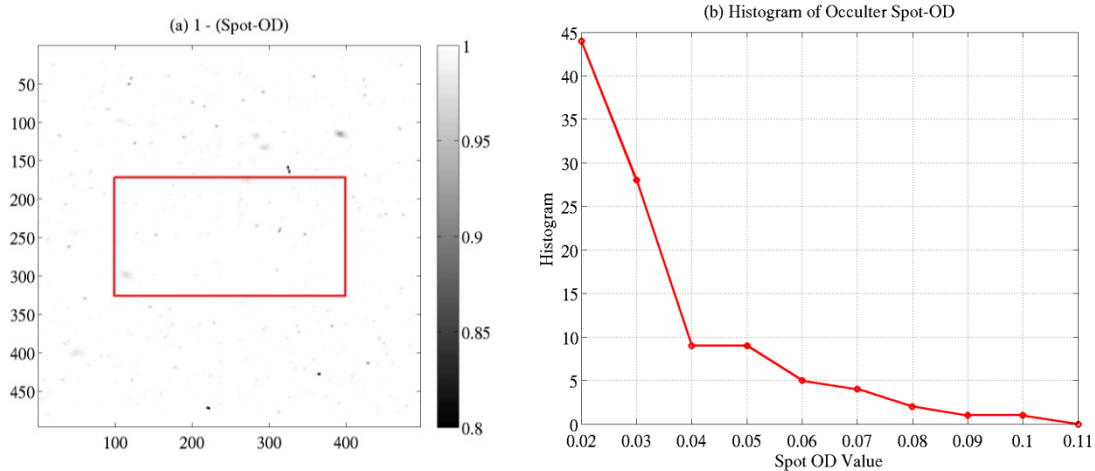
Figure 2. (a) Occulter spot map shown as $1 - $ (Spot-OD). It is obtained as follows: 1) Divide the occulter pattern out from the measured transmission amplitude. 2) Convert the resulted occulter transmittance into Optical-Density (OD), or Spot-OD. 3) Plot $1 - $ (Spot-OD). The x- and the y-axes are in pixels. (b) Histogram of Spot-OD values that are greater than 0.02 and are located inside the red-box in part (a) covering an area of [$X=\pm24\ \lambda/D$, $Y=\pm14\ \lambda/D$].
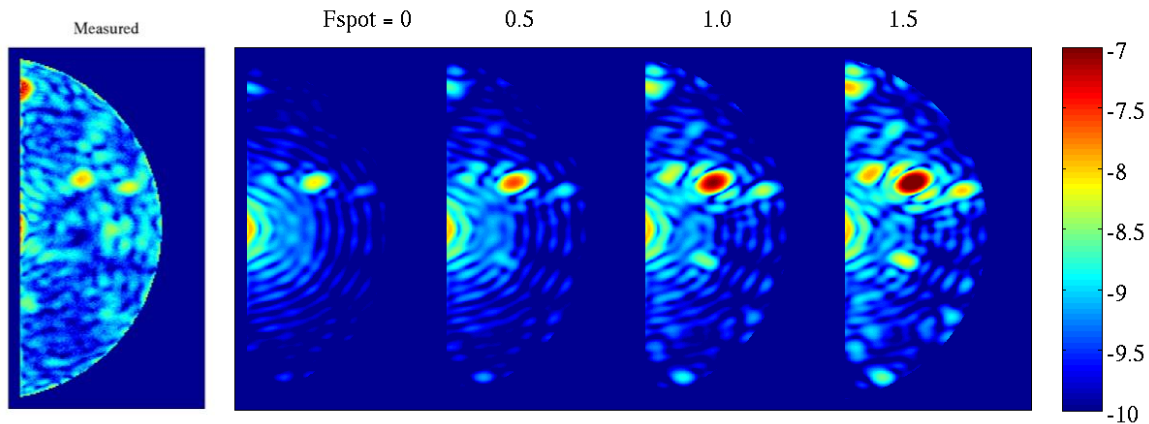

Figure 3. For the case of [$X_{\min}$, $R_{\max}$] = [3.5 20]λ/D, these figures show how the simulated contrast map changes with the value of the occulter spot-phase factor, F_{spot}. The left-most part of these plots is the measured contrast map.

In Fig. 3, we created four 10%-broadband contrast maps corresponding to different values of F_{spot} (indicated in figure title). We also included the measured composite contrast map on the left for the purpose of comparison. The composite image was formed from three 2% bandpass filters, centered at 768, 800 and 832nm spanning a 10% bandpass. (We chose three instead of all 5 bands to decrease the time to perform the experiment.) In simulations, we used 3 monochromatic beams also centered at 768, 800 and 832nm.

The contrast values corresponding to the occulter spots depend strongly on the spot OD phase. This phenomenon is quantified in Fig. 4, where the 10% broadband I_{b} values are plotted as a function of F_{spot}, and the measured I_{b} value is also included for the purpose of comparison. Although there are some differences in the features between the measured and the simulated contrast maps, the simulated contrast map obtained with $F_{\mathrm{spot}} = 1$ has a I_{b} value closest to the measured one. This is consistent with the similar situation reported in Ref. [9].

4. SENSITIVITY OF BROADBAND CONTRAST TO DARK-HOLE SIZE

In these tests, we varied the size of the dark-hole up to 24 λ/D, the theoretical limit of the 48 x 48 exposed actuators. We carried out experiments and simulations for three dark-hole sizes, Ω_{b}, with [$X_{\min}$, $R_{\max}$] = [3.5 15] and [3.5 20]λ/D in the

first two cases and with $[X_{min}, X_{max}, Y_{min}, Y_{max}] = [3.5, 24, -10, 10]\lambda/D$ in the last one. The experiments were carried out with the 768, 800, and 832 nm 2%-passband filters, with the resulting images combined to form a composite broad-band image. After determining that $F_{spot} = 1$ yields the best match in terms of broadband I_b, we carried out simulations using $F_{spot} = 1$ in all three cases. The contrast maps at 3 wavelengths and their average images over the dark-holes are shown in Fig. 5, and the corresponding I_b and I_s values are plotted in Fig. 6, where I_s is the mean value of the corresponding $I_n(x,y)$ map inside a $1\lambda/D$-wide square box centered at $X = 4.5\lambda/D$ and $Y = 0$.
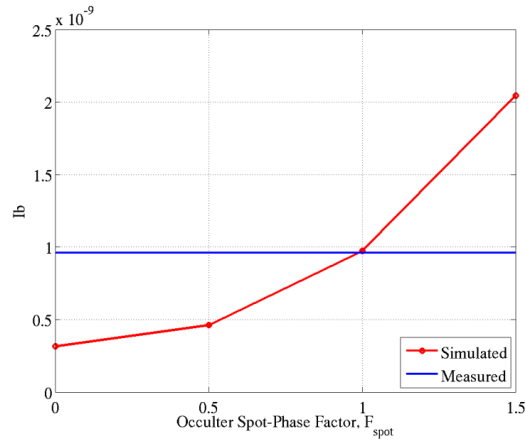

Figure 4. Simulated I_b versus F_{spot} for the case of $[X_{min}, R_{max}] = [3.5\ 20]\lambda/D$. The blue curve represents the measured I_b value.
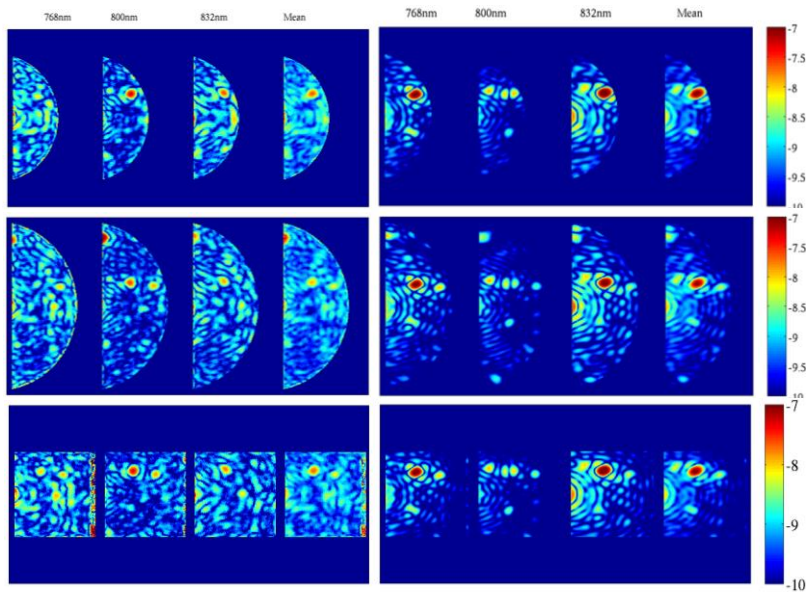

Figure 5. Left-column: Measured $I_n(x,y)$ maps at three 2%-bands and their mean corresponding to two D-shaped dark-hole areas with $[X_{min}, R_{max}] = [3.5\ 15]$ (top-row) and $[3.5\ 20]\lambda/D$ (middle-row), and one rectangular area with $[X_{min}, X_{max}, Y_{min}, Y_{max}] = [3.5, 24, -10, 10]\lambda/D$ (bottom-row). Right-column: The corresponding simulated $I_n(x,y)$ maps obtained with monochromatic beams. The corresponding I_b and I_s values are listed in Table 1, where the I_s is the mean value of $I_n(x,y)$ inside a $1\lambda/D$-wide square-box centered at $X = 4.5\lambda/D$ and $Y = 0$.

The I_b and I_s results for all three cases are summarized in Table 1. Figure 6 and Table 1 show that average dark-hole contrast is essentially independent of dark-hole size up to the Nyquist-limit of the DM used ($24\ \lambda/D$). For the full dark-hole (I_b), the worst case model agreement assuming a π phase factor at $OD=1$ is 32% (1.27×10^{-9} vs 1.88×10^{-9}). The prediction for the small dark-hole (I_s, 4-5 λ/D) is off by up to a factor of two (7.23×10^{-9} vs. 3.7×10^{-9}).
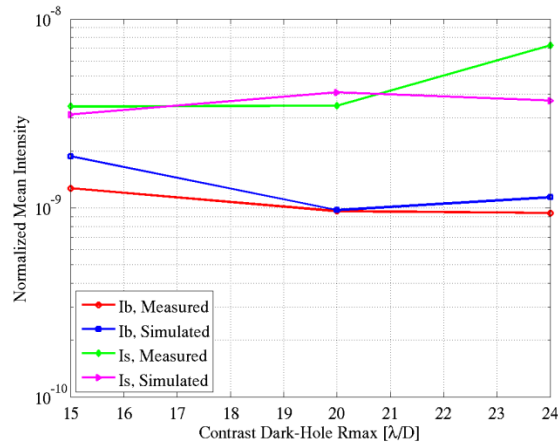
Figure 6. Measured and calculated I_b and I_s values as a function of contrast dark-hole size parameter R_{max}. In the third case, $X_{max} = R_{max}$. $F_{spot} = 1$ is used in the simulations.

Table 1. Broadband I_b - and I_s - values corresponding to three different dark-hole sizes.

Dark-Hole Size		3.5 - 15 λ/D	3.5 - 20 λ/D	3.5 - 24 λ/D, ±10 λ/D
I_b	Measured	1.27×10^{-9}	9.61×10^{-10}	9.42×10^{-10}
	Simulated	1.88×10^{-9}	9.73×10^{-10}	1.14×10^{-9}
I_s	Measured	3.44×10^{-9}	3.48×10^{-9}	7.23×10^{-9}
	Simulated	3.12×10^{-9}	4.09×10^{-9}	3.70×10^{-9}

While the contrast results and model predictions are in good agreement, we point out that the detailed prediction of speckle positions and amplitudes is not well predicted by the models. In Ref. [9], we showed in connection with Fig. 15 how the image plane pattern evolves when a set of particles is placed at different locations in the dark-hole area. To generate that figure, the measured particles were modeled as described above. The EFC algorithm was brought to convergence using a composite 10% spectrum. Then, the particle map was moved down by 21 um (about 1 λ/D) and the process was repeated. Note the dramatic change in the model prediction. Rather than seeing a fixed pattern moving through the images, the pattern evolves in an unpredictable way. We had hypothesized that the particles would 'light up' when passing over Airy rings, but this is not necessarily the case as the EFC algorithm balances the wavefront to minimize the overall contrast. This example illustrates that we cannot expect the model to be able to predict the exact amplitude and position of the speckles without a very precise knowledge of the particle distribution on the mask.

5. SENSITIVITY OF BROADBAND CONTRAST TO CONTROL BAND

The wavelength dependence of the wavefront correction is a key factor that affects the operational bandwidth as well as the time required to measure and set the wavefront. We have performed a series of tests to validate the predicted wavelength dependence of the wavefront when it is controlled in a single 2% band, or in multiple bands centered at 768, 784, 800, 816, and 832 nm. In all cases, we evaluated the contrast in all five bands and in the composite band formed by averaging the five bands with equal weighting. Most tests were carried out on 3 different days and no test was run more than one time per day. All tests were carried out in a D-shaped dark-hole extending from X=3.5 to R=11 λ/D.
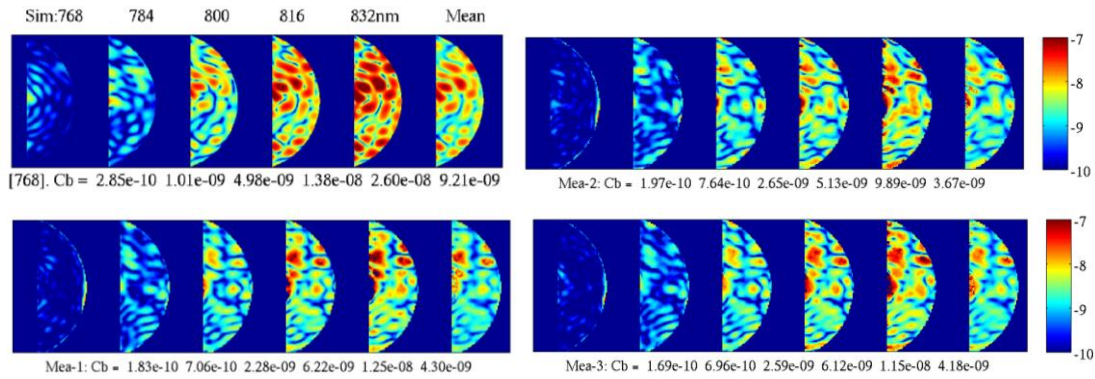
Figure 7. Simulated (top-left) and measured (the rest) $I_n(x,y)$ maps obtained by controlling the wavefront in a single 2% band centered at 768nm. In each figure, the left 5 maps are $I_n(x,y)$ corresponding to five 2%-bands centered at 768, 784, 800, 816 and 832nm, and the right-most one is their average. Listed in the x-label are the values of $I_b = C_b$, the mean values of $I_n(x,y)$ inside a D-shaped dark-hole area with $[X_{min}, R_{max}] = [3.5\ 11]\ \lambda/D$.
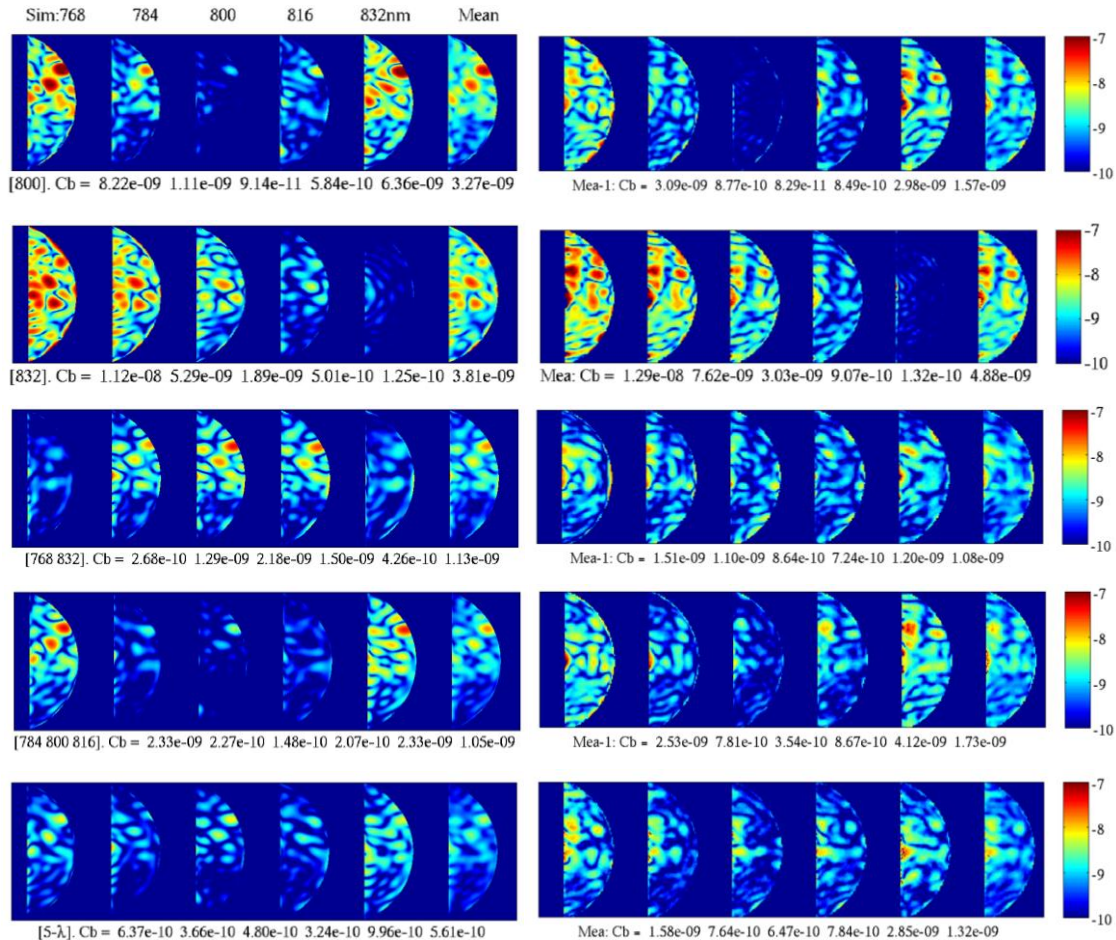

Figure 8. Simulated (left-column) and measured (right-column) $I_n(x,y)$ maps obtained by controlling the wavefront in either a single 2% band or a combination of different 2% bands centered at various wavelengths. The center(s) of the band(s) at which the wavefront is controlled is (are) indicated in the x-label of each figure shown in the left-column. In each figure, the left 5 maps are $I_n(x,y)$ corresponding to five 2%-bands centered at 768, 784, 800, 816 and 832nm, and the right-most one is their average. Listed in the x-label are the values of $I_b = C_b$, the mean values of $I_n(x,y)$ inside a D-shaped dark-hole area with $[X_{min}, R_{max}] = [3.5\ 11]\ \lambda/D$.
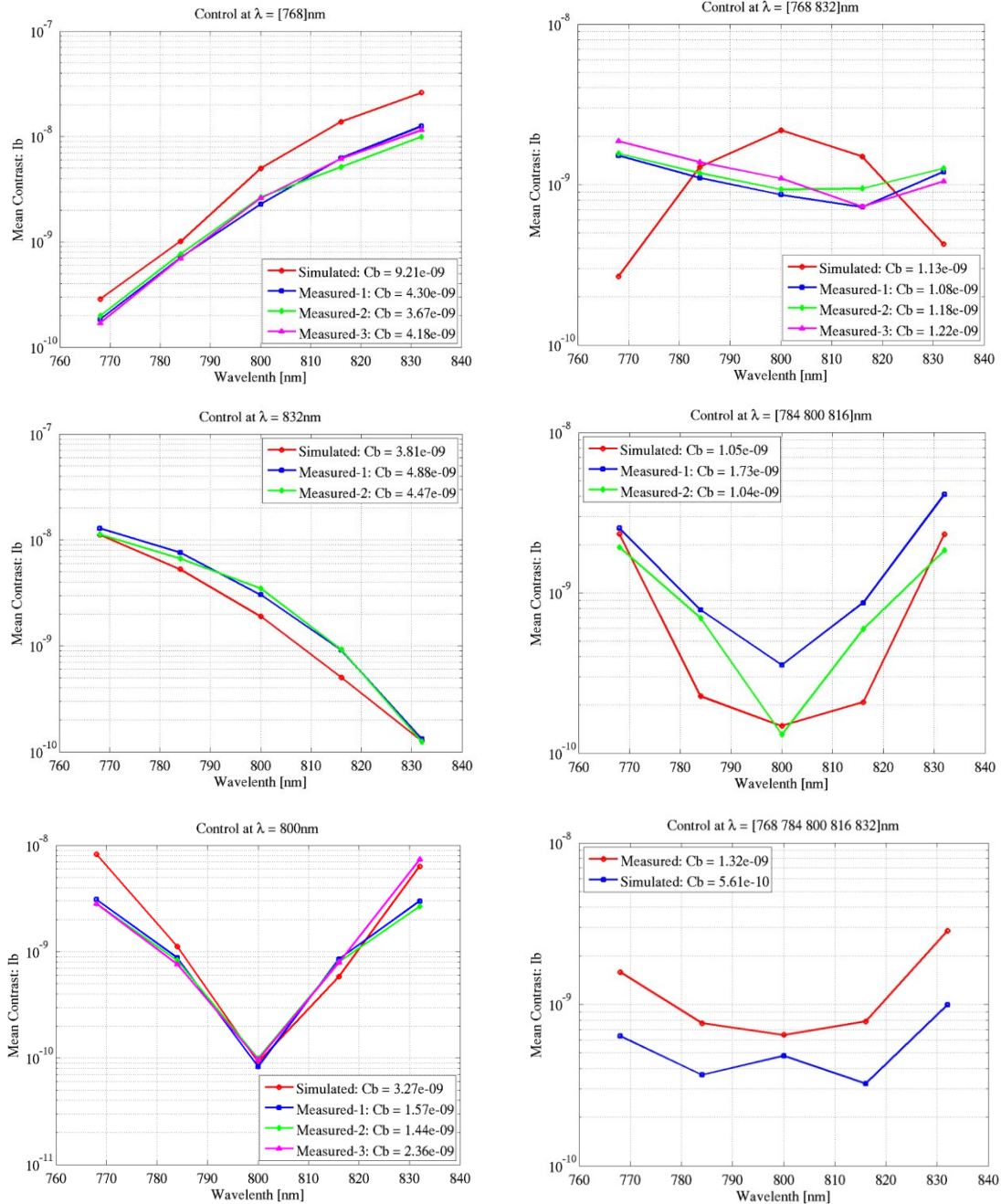
Figure 9. The mean contrast, I_b, versus the central wavelengths of five 2% bands. The multiple "measured" curves in the first 5 plots correspond to multiple test runs. The test was ran only once in the last case. Examples of $I_n(x,y)$ maps of these 6 cases are shown in Fig. 7 and Fig. 8 above.

Our model uses the measured optical density and F_{spot}=1 as described above.

We performed the following tests:

- Control at 768 nm.
- Control at 800 nm.
- Control at 832 nm.

- Control at 768 and 832 nm.
- Control at 784, 800, and 816 nm.
- Control at 768, 784, 800, 816, and 832 nm (This test was run just once.).

Results are summarized in Table 2. Simulated values in the table match the plots shown in Fig.7 and Fig. 8. For measured values, we used the mean of the multiple runs in all cases except the last one, i.e., control at 768, 784, 800, 816, and 832 nm, where the test was run just once. In Fig.7, we show the predicted $I_n(x,y)$ map as well as the measured $I_n(x,y)$ maps of the three runs obtained by controlling the wavefront at 768nm. This figure is included here as an example of multiple measurement runs at each control band. In Fig. 8, we show the simulated and the measured $I_n(x,y)$ maps of the remaining 5 cases of control band. In this plot, we included only one set of measured $I_n(x,y)$ maps for each case of control band. Shown in Fig. 9 are the values of I_b listed in the x-labels of the plots in Fig. 7 and Fig. 8, as well as those of the measured maps not presented in this paper.

It is interesting to compare the two cases where the upper and lower wavelengths are controlled. When the 832 nm wavelength is controlled, the model accurately predicts the contrast in the 768 nm band. But when controlling in the 768 band, the model overestimates the 832 nm band. Furthermore, when controlling in the middle of the band, the model overestimates the 768 band but accurately predicts the 832 band.

The model predictions for simultaneous control at the 768 and 832 bands are intuitive; the contrast is best at those extreme bands, and worse in the middle. Yet the testbed did not behave this way at all. The middle bands had slightly better contrast than the ends. We do not understand why this happened.

Another significant difference between the model and the experiment is seen in the control at 3 bands, 784, 800, and 816. Here, the model predicts what looks like a quadratic increase in contrast (in the log plots) from the central band outward. But the experiment shows that the contrast increases linearly (again, in log space).

When controlling in all 5 bands, the general behavior is correct, but the model predicts that the 784 nm and 816 nm bands will have the best contrast, while the experiment showed that 800 nm was best. This, at least, is consistent with the 3 band test where the model predicted better behavior for 816 and 784 than was seen in the experiment.

Table 2. Summary of control bandwidth results.

Contrast x 1e-9

Control Band		768	784	800	816	832	Mean
	Measured Data	0.18	0.72	2.51	5.82	11.29	4.05
768	Simulated Data	0.285	1.01	4.98	13.8	26	9.21
	|Meas - Sim|	0.11	0.29	2.47	7.98	14.71	5.16
	Measured Data	2.91	0.82	0.009	0.81	4.33	1.79
800	Simulated Data	8.22	1.11	0.0914	0.584	6.36	3.27
	|Meas - Sim|	5.31	0.29	0.08	0.23	2.03	1.48
	Measured Data	12.07	7.15	3.26	0.91	0.13	4.67
832	Simulated Data	11.2	5.29	1.89	0.501	0.125	3.81
	|Meas - Sim|	0.87	1.86	1.37	0.41	0.01	0.86
	Measured Data	1.65	1.22	0.96	0.8	1.17	1.16
768 and 832	Simulated Data	0.268	1.29	2.18	1.5	0.426	1.13
	|Meas - Sim|	1.38	0.07	1.22	0.70	0.74	0.03
	Measured Data	2.23	0.74	0.24	0.73	2.98	1.38
784, 800, and 816	Simulated Data	2.33	0.227	0.148	0.207	2.33	1.05
	|Meas - Sim|	0.10	0.51	0.09	0.52	0.65	0.33
768, 784, 800, 816, and 832	Measured Data	1.58	0.76	0.65	0.78	2.85	1.324
	Simulated Data	0.64	0.37	0.48	0.32	1	0.562
	|Meas - Sim|	0.94	0.39	0.17	0.46	1.85	0.76

6. CONCLUSION

We have found in our previous work [9] that the average value, general nature, and chromatic behavior of the dark hole floor is explained by a model based on the measured occulter transmittance image after introducing additional phase values to all major occulter spots. Our studies presented in this paper reinforce these findings. That is, mask contaminants or defects, such as partially-transmitting spots with large parasitic phases, were the performance-limiting factor. We measured the mask transmission in a microscope and in the testbed using a diffuser. We added an empirical phase $\pi \times OD$ radians, and this led to models that can predict well the broad-band behavior and the coherent contrast floor of our HCIT testbed.

In this paper we presented results on our theoretical and experimental studies of the sensitivity of dark-hole contrast to the control bandwidth and dark-hole dimensions in our HCIT testbed. We showed good agreement between measurement and simulations, with one major and unexplained difference that the experiment and model diverged when we controlled only at the two end points in wavelength. This result remains unexplained.

In a companion paper we have reported on model and data agreement for non-functional DM actuators [10]. These experimental validations of key coronagraph sensitivity factors will additionally contribute to the confidence in performance prediction models for future flight systems.

REFERENCES

[1] John T. Trauger, Chris Burrows, Brian Gordon, Joseph J. Green, Andrew E. Lowman, Dwight Moody, Albert F. Niessner, Fang Shi, and Daniel Wilson, "Coronagraph contrast demonstrations with the high-contrast imaging testbed," Proc. SPIE 5487, 1330 (2004).

[2] Andrew E. Lowman, John T. Trauger, Brian Gordon, Joseph J. Green, Dwight Moody, Albert F. Niessner, and Fang Shi, "High-contrast imaging testbed for the Terrestrial Planet Finder coronagraph," Proc. SPIE 5487, 1246 (2004).

[3] Erkin Sidick, Fang Shi, Scott Basinger, Dwight Moody, Andrew E. Lowman, Andreas C. Kuhnert, and John T. Trauger, "Performance of TPF's High-Contrast Imaging Testbed: Modeling and simulations," Proc. SPIE 6265, 62653L (2006).

[4] Amir Give'on et al, "Broadband wavefront correction algorithm for high-contrast imaging system," Proc. SPIE 6691, 66910A (2007).

[5] Modeling and Analysis for Controlled Optical Systems User's Manual, Jet Propulsion Laboratory, California Institute of Technology, Pasadena, CA.

[6] Erkin Sidick, Stuart Shaklan, Amir Give'on, and Brian Kern, "Studies of the effects of optical system errors on the HCIT contrast performance," Proc. SPIE 8151, 8151-06 (2011).

[7] Erkin Sidick, Stuart Shaklan, John Krist, Eric J. Cady, and Brian Kern, "HCIT contrast performance sensitivity studies: Simulation versus experiment," Proc. SPIE 8864, 88640Q-1 (2013).

[8] Erkin Sidick, Stuart Shaklan, and Kunjithapatham Balasubramanian, "HCIT broadband contrast performance sensitivity studies," Proc. SPIE 8520, 85200M-1 (2012).

[9] Erkin Sidick, Stuart Shaklan, Kunjithapatham Balasubramanian, and Eric Cady "High-contrast coronagraph performance in the presence of focal plane mask defects," Proc. SPIE 9143, 914336-1 (2014).

[10] Erkin Sidick, Stuart Shaklan, and Eric Cady, "High-contrast coronagraph performance in the presence of DM actuator defects," Proc. SPIE 9605, 9605-68 (2015).